ACS APPLIED MATERIALS & INTERFACES

Research Article

www.acsami.org

# Dopant-Controlled Morphology Evolution of $WO_3$ Polyhedra Synthesized by RF Thermal Plasma and Their Sensing Properties

Mingshui Yao,[†,‡] Qiaohong Li,[‡] Guolin Hou,[†,§] Chen Lu,[†,§] Benli Cheng,[†] Kechen Wu,[‡] Gang Xu,[‡] Fangli Yuan,*[,†] Fei Ding,*[,†] and Yunfa Chen[†]

[†]State Key Laboratory of Multi-Phase Complex Systems, Institute of Process Engineering, Chinese Academy of Sciences (CAS), Zhongguancun Beiertiao 1 Hao, Beijing 100190, China

[‡]State Key Laboratory of Structural Chemistry, Fujian Institute of Research on the Structure of Matter, Chinese Academy of Sciences (CAS), 155 Yangqiao Road West, Fuzhou, 350002, P. R.China

[§]University of Chinese Academy of Sciences (UCAS), No. 19A Yuquan Road, Beijing 100049, China

Supporting Information

**ABSTRACT:** In this paper, a simple way is developed for the synthesis of Cr-doped $WO_3$ polyhedra controlled by tailoring intrinsic thermodynamic properties in RF thermal plasma. Scanning electron microscopy, transmission electron microscopy, X-ray diffraction, and X-ray photoelectron spectroscopy are used to characterize the detail structures and surface/near-surface chemical compositions of the as-prepared products. Kinetic factors showed little effects on the equilibrium morphology of Cr-doped $WO_3$ polyhedra, while equilibrium morphologies of $WO_3$ polyhedra can be controlled by the thermodynamic factor (Cr doping). Set crystal growth habits of pure $WO_3$ as an initial condition, coeffects of distortions introduced by Cr into the $WO_3$ matrix, and a chromate layer on the crystal surface could reduce the growth rates along [001], [010], and [100] directions. The morphology evolution was turning out as the following order with increasing Cr dopants: octahedron−truncated octahedron−cuboid. 2.5 at. % Cr-doped $WO_3$ polyhedra exhibit the highest sensing response due to coeffects of exposed crystal facets, activation energy, catalytic effects of Cr, and particle size on the surface reaction and electron transport units. By simply decorating Au on Cr-doped $WO_3$ polyhedra, the sensing responses, detection limit, and response−recovery properties were significantly improved.

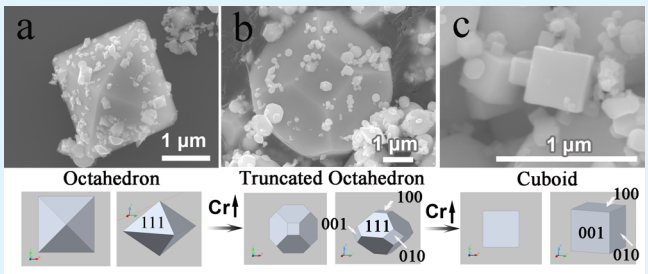


**KEYWORDS:** *$WO_3$, dopant, crystal growth habit, RF thermal plasma, MOX sensors*

## 1. INTRODUCTION

Crystals with different types of exposed facets usually exhibit various physical and chemical properties; such anisotropy is one of the basic properties of crystals.[1] The final shape of a crystal and the exposed facets are a result of the interplay between thermodynamics (e.g., selective adsorption of capping or stabilizing reagents[2,3]) and kinetics (e.g., the crystal growth rate during the nucleation and growth of crystals[4,5]). However, the understanding of the synthesis of crystals with specific facets and the relationship between activity and surface structure is still limited,[1] especially for those synthesized by chemical vapor deposition (CVD). In addition, the dopant-controlled octahedron-to-cuboid morphology evolution of $WO_3$ crystals has not been reported so far.

Since the temperature of the flame is ultrahigh (up to $10^4$ K), nuclei are formed without substrates/catalysts, and the supply of atoms to the nuclei are almost equal in all directions, the crystal thermal equilibrium morphologies in RF thermal plasma are in fact determined by crystal growth habits (intrinsic thermodynamic properties) and in some cases affected by kinetic factors when the growth rate of the crystal is sensitive. We have successfully prepared ZnO nanowires, ZnS nanobelts, and $WO_3$ octahedra with specific exposed facets via RF thermal plasma method[6−8] and found that the morphologies of ZnO and ZnS with sensitive [001] growth direction could be changed by kinetic factors, while the morphology of $WO_3$ could only be determined by its crystal growth habit.

$WO_3$ is a transition metal oxide with wide range of applications such as photocatalysis,[9−12] gas sensors,[7,13] anode materials of Li-ion batteries,[14] supercapacitors,[15] field emitters,[16] electrochromic (EC) devices,[17,18] and so on. To obtain nanostructures with specific exposed facets and hierarchical structures, tungsten oxides were synthesized using varying techniques to form zero-dimensional (0D),[3,7,19,20] 1D,[21,22] 2D,[13,23,24] and $0^{25}/1^{26}$/2D-based[27,28] hierarchical structures. Among these, morphology-controlled syntheses of 0D $WO_3$ crystals with exposed specific facets are of great significance to

Received: November 19, 2014
Accepted: January 12, 2015
Published: January 12, 2015





DOI: 10.1021/am5081277
ACS Appl. Mater. Interfaces 2015, 7, 2856−2866

the understanding of both their synthesis and the relationship between activity and surface structure.

In RF thermal plasma, $WO_3$ products without dopants showed octahedral shapes with {111} exposed facets due to fast growth rate along [001], [010], and [100] directions.[7] Doping might be an ideal candidate to tailor exposed facets of $WO_3$ due to its potential for affecting the crystal growth habit (i.e., growth rates along different crystal directions). Cr-$WO_3$ with polyhedral shape and tunable exposed specific facets cannot be achieved either by liquid phase methods or other vapor phase methods so far. Herein, a study of the doping effect of Cr elements on the shape of $WO_3$ polyhedra synthesized by RF thermal plasma was demonstrated. The morphologies were controlled by tailoring the corresponding crystal growth habits via Cr doping. With increasing Cr dopants, the morphologies changed according to the following order: octahedron−truncated octahedron−cuboid. The gas sensing properties were also studied here.

## 2. MATERIALS AND METHODS

**2.1. Preparation of the Precursor: Cr-APT.** The precursors of Cr-doped $WO_3$ polyhedra were obtained according to the following steps. First, 300 g of ammonium paratungstate tetrahydrate powder (APT, Ganzhou Tejing Tungsten and Molybdenum Co.,Ltd., China) was mixed with 37 mL of aqueous solution of ammonium chromate (~0.70 M for 2.5 at. % sample, Beijing Chemical Co., Ltd., China). Then the mixture was moved to a vacuum oven (40 °C) for 12 h, and the dried mixture was ground in a mortar and passed through a 100-mesh sieve repeatedly. The final mixture was marked as Cr-APT. It should be noted that the surface area of APT limits the amount of ammonium chromate coated on its surface (up to 10 at. %). Higher than 10 at. % will result in the mixture of Cr-APT and ammonium chromate powders.

**2.2. Synthesis of Cr-Doped $WO_3$ Polyhedra, $Cr_2O_3$, and $WO_3$ Octahedra.** The syntheses of Cr-doped $WO_3$ polyhedra, $Cr_2O_3$, and $WO_3$ octahedra were carried out in an RF thermal plasma system under atmospheric pressure. The schematic illustration of the system is available in in our previous works,[7,29] and the modified product collecting system is shown in Figure 1a.

The reactor consists of a vertical quartz tube of 5 cm diameter and 15 cm length. Cr-APT/ammonium paratungstate tetrahydrate/APT was subjected to thermal decomposition in Ar−$O_2$ plasma as received, and the produced Cr-doped $WO_3$ polyhedra/$Cr_2O_3$/ $WO_3$ octahedra were collected at the bottom of the chamber (Figure 1a). The detailed parameters for the plasma processing are given in Table 1.

**2.3. Synthesis of Au-Decorated 2.5 at. % Cr-Doped $WO_3$ Polyhedra.** The synthesis of Au-decorated 2.5 at. % Cr-doped $WO_3$ polyhedra was modified from the report of Zhang et al.[30] First, 0.20 g of 2.5 at. % Cr-doped $WO_3$ polyhedra was dispersed in 60 mL of $HAuCl_4$ (1 mM) aqueous solution under stirring, and 20 mL of $NH_3 \cdot H_2O$ (3 M) was added. After stirring for about 3 h, the precipitate was collected by centrifugation at 4000 rpm and washed with deionized (DI) water and absolute ethanol for several times and then dried at 80 °C for 4 h. The resulting brown precursor was annealed at 350 °C for 1 h, and the Au-decorated 2.5 at. % Cr-doped $WO_3$ polyhedra with a purple-brown color were finally obtained.

**2.4. Materials Characterization.** The phase and crystal structures of the products were determined by X-ray diffraction (XRD) patterns, which were recorded with a Philips X'Pert PRO MPD X-ray diffractometer using Cu K$\alpha$ radiation ($\lambda$ = 1.541 78 Å). The morphology and structure of the product were then observed by scanning electron microscope (SEM, JEOL JSM-6700F) and transmission electron microscope (TEM, JEOL JEM-2100). $N_2$ adsorption was measured by a BET instrument using a surface area analyzer (NOVA3200e, Quantachrome, U.S.A.). The particle size distribution of the synthesized powder was determined using a Beckman Coulter LS 13 320 laser-diffraction particle size analyzer. The surface chemical analysis was investigated by X-ray photoelectron spectroscopy (XPS) on a Thermo Scientific ESCALAB 250 Xi XPS system, where the analysis chamber was 1.5 × $10^{-9}$ mbar and the size of X-ray spot was 500 $\mu$m.

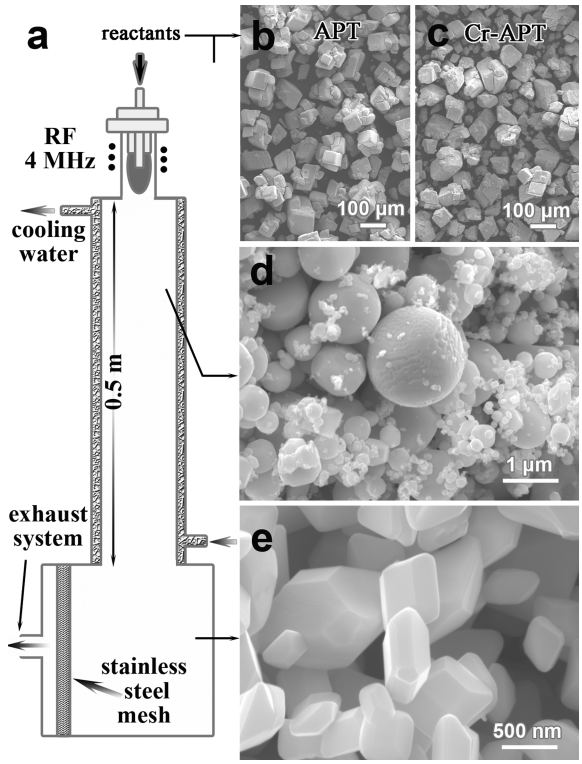


**Figure 1.** (a) Schematic diagram of the RF-induced plasma setup and SEM images of (b) APT, (c) Cr-APT, (d) particles collected from the upper part of the chamber, and (e) particles collected from the bottom collector.

**Table 1. Parameters of Ar−$O_2$ Plasma Processing**

| parameters | values |
|---|---|
| plasma power | 15 kW |
| central gas, argon | 0.6 $m^3$ $h^{-1}$ |
| sheath gas, oxygen | 2.0 $m^3$ $h^{-1}$ |
| carrier gas, oxygen | 0.3−0.6 $m^3$ $h^{-1}$ |
| negative pressure | 50−100 mm $H_2O$ |
| powder feeding rate | 5−20 g $min^{-1}$ |

**2.5. Fabrication of Gas Sensor Prototype and Sensor Characterization.** The fabrication of gas sensor prototypes and the sensor characterization were reported in our previous works.[29,31] Briefly, the solution containing sensing material and ethanol was drop-coated onto the $Al_2O_3$ substrate with two Ag electrodes. Then the sensor was preheated at 550 °C for 2 h and stabilized at 400 °C for 20 h to ensure good ohmic contact. Target gas was introduced into the quartz tube by mixing the certified gas ""mixtures"" and dry air in the proper ratio controlled by the mass flow controllers.[32] The constant flow was 600 mL $min^{-1}$, the bias on the sensor was 5 V, and the current was recorded using Keithley 2601 Sourcemeter. The response was defined as the ratio of sensor resistance in air and in detected gas ($R_{air}/R_{gas} - 1$). The response time was defined as the time required for the resistance of the sensor to change to 90% of the saturation value after exposure to the test gas.

## 3. RESULTS AND DISCUSSION

**3.1. Materials Preparation and Characterization.** Figure 1 shows the schematic illustration of the RF-induced plasma setup and the corresponding SEM images of the reactants and the products collected at different parts of the


DOI: 10.1021/am5081277
ACS Appl. Mater. Interfaces 2015, 7, 2856−2866

system (2.5 at. % Cr-doped $WO_3$ as an example). It can be seen that both APT and Cr-APT are separate particles with a diameter of hundreds of micrometers and good flowability, which is beneficial to the continuous feed.

*3.1.1. Effect of Kinetic Factors.* Affected by the quenching rate, an important kinetic factor for vapor phase method, products collected showed two types of morphologies, which were spheres and crystals with specific exposed facets (Figure 1d and e). It is well-known that the lowest energy surface for a liquid droplet is a sphere. The quenching rate was ultrahigh for the powders formed in the upper part of the chamber (surrounded by cooling water); therefore, the surface atoms of the condensed spherical droplets lose their energy very fast and do not move around,[20,33] which resulted in the formation of spherical particles. In contrast, the surface atoms of the particles condensed at a low quenching rate lost their energy slowly, and equilibrium forms were formed. The equilibrium forms were found to be polyhedra with regular shapes (truncated octahedra for 2.5 at. % Cr-doped $WO_3$). Considering differences in dwell time in high-temperature region for further crystal growth, it is easy to understand that rapid quenching in the upper part of the chamber resulted in smaller mean size (0.52 $\mu$m) and less stable phase (61 wt %, $\gamma$-$WO_3$, semiquantitative concentration calculated by X'pert Highscore software) than those formed by slow quenching (0.69 $\mu$m and 73 wt %, Table 2).

**Table 2. Effects of Some Kinetic Factors on the Morphology and Crystal Phase of 2.5 at. % Cr-Doped $WO_3$**

| quenching rate | powder feeding rate (g $min^{-1}$) | sheath gas, oxygen ($m^3$ $h^{-1}$) | carrier gas, oxygen ($m^3$ $h^{-1}$) | mean size ($\mu$m) | stable phase (wt %) |
|---|---|---|---|---|---|
| slow | 5 | 2.0 | 0.3 | 0.69 | 73 |
| rapid | 5 | 2.0 | 0.3 | 0.52 | 61 |
| slow | 20 | 2.0 | 0.3 | 0.60 | 80 |
| slow | 5 | 2.0 | 0.6 | 0.56 | 71 |

[a]Stable phase refers to semiquantitative concentration wt % of $\gamma$-$WO_3$ calculated by X'pert Highscore software

Other kinetic factors showed little effects on the equilibrium morphology of 2.5 at. % Cr-doped $WO_3$. For example, by increasing the amount of Cr-APT subjected into the plasma jet from 5 to 20 g $min^{-1}$, the obtained products showed more stable phase (80 wt %) and smaller mean size (0.60 $\mu$m) without changing equilibrium morphology. As we know, the nucleation rate increases with the increasing supersaturation, and thus large numbers of nuclei were formed and grew homogeneously; this led to narrow particle distribution and small mean size. More stable phase might be ascribed to vigorous decomposition and small size (effective annealing).

We decreased the dwell time of the particles in the high-temperature region by increasing the flow rate of carrier gas. It resulted in smaller mean size (0.56 $\mu$m) and less stable phase (71 wt %) due to less time for further crystal growth and annealing, respectively. The equilibrium morphology of 2.5 at. % Cr-doped $WO_3$ remained unchanged.

*3.1.2. Effect of Thermodynamic Factors (Cr Dopants).* Since kinetic factors cannot changed the equilibrium morphologies of Cr-doped $WO_3$ products, the effects of thermodynamic factors were studied. However, common methods such as selective adsorption of capping or stabilizing agents cannot be realized in RF thermal plasma. Therefore, doping would be an ideal method to tailor the equilibrium morphologies of Cr-doped $WO_3$ products due to its potential for affecting the crystal growth habit (i.e., growth rates along different crystal directions).

*3.1.2.1. Effect of Thermodynamic Factors on Morphology Evolution (Cr Dopants).* The crystallographic structures of the products were investigated by XRD and showed the typical patterns of the standard monoclinic $\gamma$-$WO_3$ (Figure 2a, JCPDS No. 00-083-0950, also named as monoclinic I). A metastable weak phase called $\varepsilon$-$WO_3$ (JCPDS No. 01-087-2404) was also observed (Figure 2b and d). The intensities of diffraction peaks declined as Cr concentration increased, indicating that Cr dopants within $WO_3$ caused degeneration of the crystallinity (Figure 2a–c). It can be seen that Cr dopants also reduce the intensities of (002) and (200) peaks and finally result in the fact that the intensities of (002), (020), and (200) are close to each other, which reflects changes in morphology. Figure 2 also shows that Cr-doped $WO_3$ products were prepared without the formation of a new phase.

It can be seen in Figure 2a–c that Cr dopant slightly shifts the positions of XRD peaks to higher diffraction angles, which is consistent with Cr-doped $WO_3$ particles reported by other researchers.[34] The only exception is 10 at. % sample, which might due to its poor crystallinity (Figure 2b, light blue). Similar phenomenon was observed when 2.5 at. % sample with poor crystallinity (collected from the upper part of the chamber) was measured (Figure 2d, green).

Figure 3 shows the Raman spectra of as-synthesized and heat-treated products, respectively. In these spectra, peaks at 272, 324, 715, and 805 $cm^{-1}$ correspond to $\gamma$ phase[35] and peaks at 203, 272, 303, 370, 425, 642, 688, and 805 $cm^{-1}$ belong to the $\varepsilon$ phase.[36] The bands at 942 and 992 $cm^{-1}$ can be assigned to the stretching mode of W═O terminal[35] and Cr═O terminal bonds of dehydrated monochromates,[37] respectively, indicating the existence of surface tungsten hydrates and the existence of chromium, respectively. $\varepsilon/\gamma$ phase ratio in the products by Raman spectra is consistent with XRD results.

Based on our previous work on $WO_3$ octahedra[7] and detailed characterizations of undoped and Cr-doped $WO_3$ polyhedra, we summarized the morphology evolution and the corresponding crystal growth habits in Figure 4.

As shown in Figure 4a, d, and g, $WO_3$ products without dopants showed octahedral shapes with {111} exposed facets due to fast growth rate along [001], [010], and [100] directions. The well-defined uniform octahedral structure shows a highly symmetric and regular shape containing 8 facets, 6 vertices, and 12 edges, which exhibits sharp edges and corners as well as smooth surfaces. All of the products with different sizes (nano-/submicro-/microscale) show the same octahedral morphology based on the SEM and TEM images in different magnifications.

It can be seen in Figure 4b, e, and h that lattices of 0.38 nm (insets of Figure 4h) were indexed as [001] and [010] directions of $\gamma$-$WO_3$, which confirms that the equatorial plane perpendicular to the zone axis was (100). Therefore, the introduction of low concentration of Cr dopants to the lattice of $WO_3$ led to the formation of truncated octahedra with {111}, (001), (010), and (100) exposed facets by significantly reducing the growth rates along [001], [010], and [100] directions. SEM and TEM images in different magnifications show that the sizes of truncated octahedral Cr-$WO_3$ have a range from tens of nanometres to a few microns.


DOI: 10.1021/am5081277
ACS Appl. Mater. Interfaces 2015, 7, 2856–2866

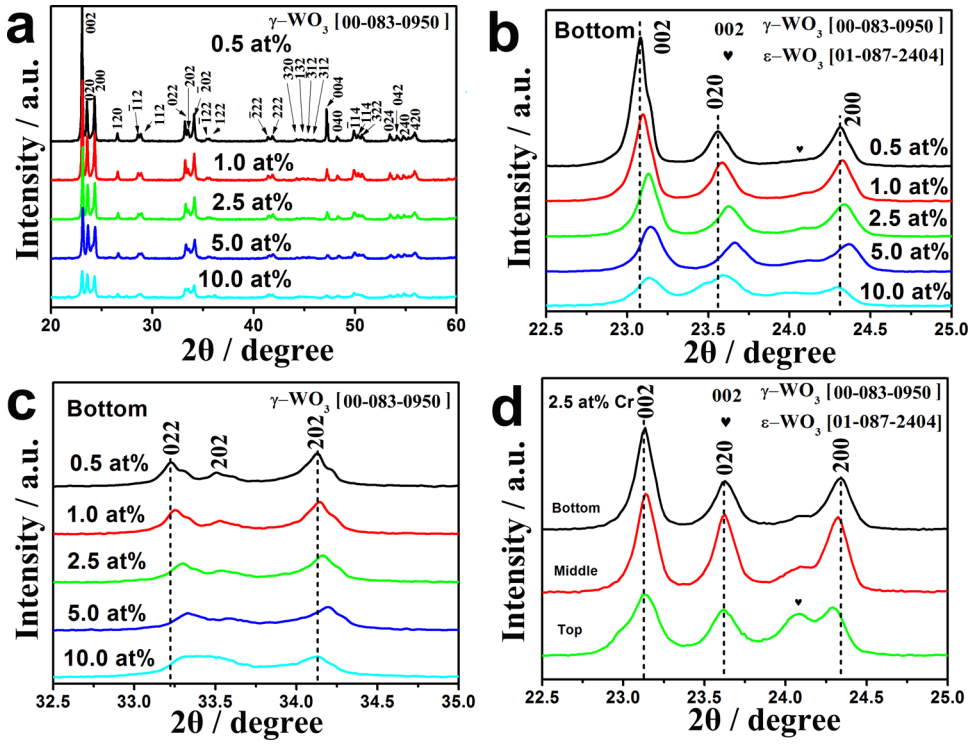


**Figure 2.** XRD patterns of (a–c) $WO_3$ products (bottom) doped with different atomic percentage of Cr and (d) $WO_3$ products collected at different parts of the reactor.

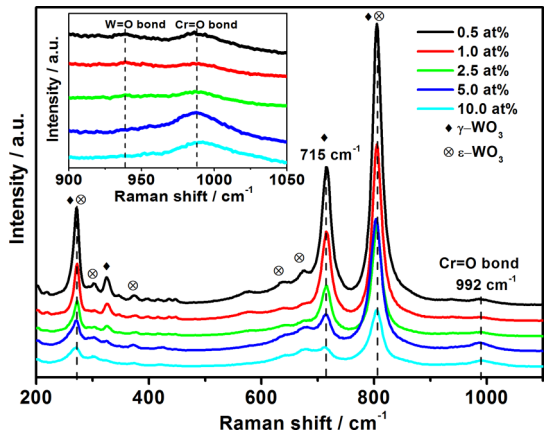


**Figure 3.** Raman spectra of $WO_3$ products (bottom) doped with different atomic percentage of Cr (the inset is high magnification of Raman patterns from 900 to 1050 $cm^{-1}$).

Further introduction of Cr dopants (up to 10.0 at. %) sharply reduced the growth rates along [001], [010], and [100] directions to the slowest one and formed cuboids with (001), (010), and (100) exposed facets (Figure 4c, f, and i, range from a few nanometers to hundreds of nanometers).

*3.1.2.2. Effect of Thermodynamic Factors on Size Distributions (Cr Dopants).* The size distribution and the size evolution of Cr-$WO_3$ polyhedra were also studied. The sizes of all of the samples are mainly less than 1.0 $\mu$m as shown in Figure 5a. The increasing percentage of nanometer-size part and decreasing percentage of micrometer-size part indicate that the introduction of Cr dopants prevents the further growth of the crystals. As a result, the median particle diameter (D50) and the mean size of Cr-$WO_3$ polyhedra decrease with increasing the amounts of Cr dopants (Figure 5b). The median particle diameter (D50) and mean size of 2.5 at. % Cr-doped $WO_3$ truncated octahedral were measured to be 0.23 and 0.69 $\mu$m, respectively. The BET surface areas were estimated to be 4.88 (0 at. %),[7] 5.71 (0.5 at. %), 6.28 (1.0 at. %), 6.76 (2.5 at. %), 7.26 (5.0 at. %), and 8.08 $m^2\ g^{-1}$ (10 at. %), respectively (blue, Figure 6b). The mean size of Cr-$WO_3$ polyhedra calculated from BET surface areas decreases from 0.15 to 0.10 $\mu$m (green, Figure 6b, for details, see Supporting Information). The difference in mean sizes obtained by the two methods can be explained by the agglomeration of the particles as well as their motion in aqueous solution that contributed to larger particle size results by the laser-diffraction particle size analyzer.

*3.1.3. Detailed Characterization of 2.5 at. % Cr-Doped $WO_3$ Truncated Octahedra.* EDS mapping images of 2.5 at. % Cr-doped $WO_3$ truncated octahedra in Figure 6a indicate that Cr dopants are uniformly distributed in the particle, and its atomic percentage was calculated to be 1.73%. The surface/near-surface chemical composition of 2.5 at. % Cr-doped $WO_3$ was examined by X-ray photoelectron spectroscopy (XPS). The full-range XPS spectrum (Figure 6b) reveals that it is mainly composed of W, Cr, O, and C elements, of which C can be mainly attributed to external contaminations during products collection (including adsorption contaminations on the nanoparticles surface due to exposure to ambient air[38]). More detailed information on the chemical state of these elements can be obtained from the high-resolution XPS spectra of the W 4f, Cr 2p, and O 1s in Figure 6c–e. The peaks of W $4f_{7/2}$ at 35.7 eV can be assigned to the existence of the $WO_3$ chemical state at the surface.[38,39] The binding energies for metallic tungsten, $WO_2$, and $WO_3$ were reported to be 31.3, 32.7, and 35.7–36.1 eV, respectively.[40] Various chromium oxides can be distinguished from each other by XPS. The binding energy (BE) of Cr $2p_{3/2}$ is 577.1 eV, the Cr $2p_{3/2}$–Cr $2p_{1/2}$ BE separation is 9.8 eV, and O 1s is 530.3 eV. Since both of them


DOI: 10.1021/am5081277
ACS Appl. Mater. Interfaces 2015, 7, 2856–2866

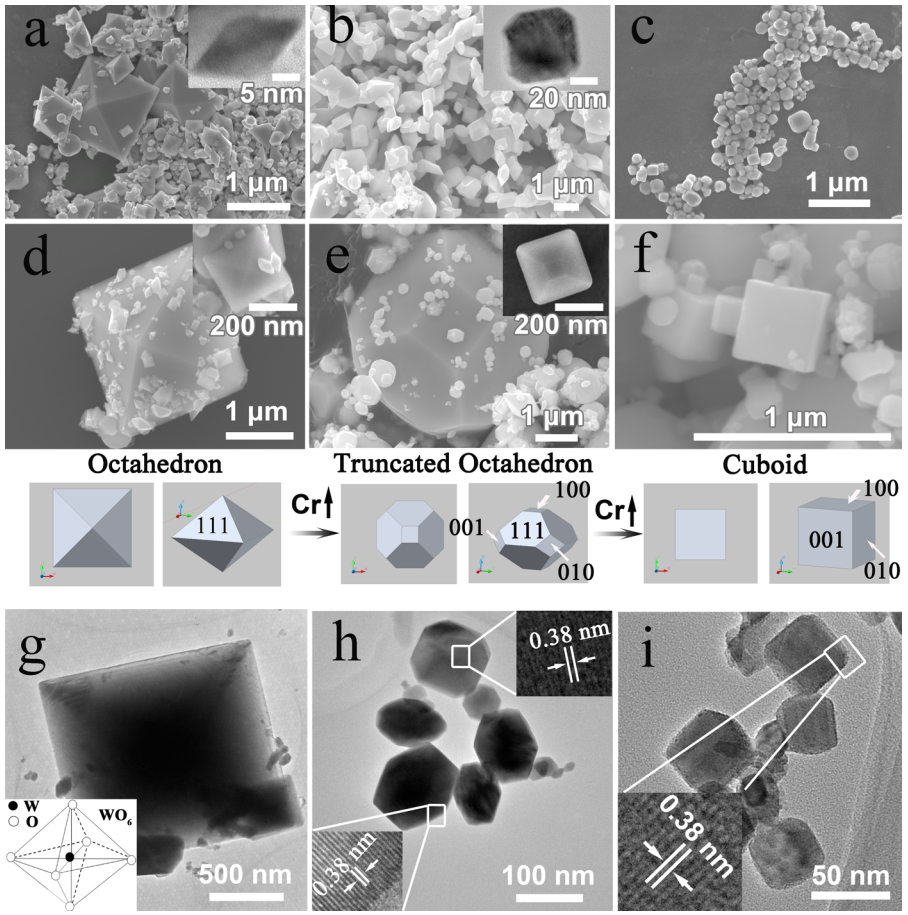


**Figure 4.** Summarization of morphology evolution and the corresponding crystal growth habits (middle part is the corresponding schematic illustration): SEM images (insets of a and b are the corresponding HRTEM images of nanoparticles, insets of d and e are the corresponding high-manification SEM images of submicroparticles) of (a, d) $WO_3$, (b, e) 2.5 at. % Cr-$WO_3$ and (c, f) 10.0 at. % Cr-$WO_3$; TEM images (insets of h and i are the corresponding HRTEM images) of (g) $WO_3$ (the inset is a schematic diagram of $WO_6$ octahedron), (h) 2.5 at. % Cr-$WO_3$, and (i) 10.0 at. % Cr-$WO_3$.

are consistent with $Cr_2O_3$,[41−43] the oxidation state of the dopant can be assigned to $Cr^{3+}$. Calculated from the quantified peak area, the atomic ratio of Cr/W is estimated to be about 2.83 at. % (XPS), which is a little higher than that estimated by EDS (1.73 at. %). It is consistent with the discussion mentioned above that the majority of the Cr atoms exist in the form of Cr═O terminal bond and thus a chromate layer formed on the crystal surface of $WO_3$ polyhedron.

*3.1.4. Possible Growth Mechanism.* The structure of the stable monoclinic $WO_3$ is $ReO_3$-type (corner sharing arrangement of $WO_6$ octahedra). Similarly, $\gamma$-$WO_3$ is also formed by corner sharing of $WO_6$ octahedra. $WO_6$ octahedron can be described as follows (the inset of Figure 4g): W ions occupy the corners of a primitive unit cell, O ions bisect the unit cell edges, and each W ion is surrounded by six equidistant oxygen ions. The main differences between different phases are the positions of the W ions within the octahedron and lengths of W−O bonds.

Surface energies and formation energies were calculated for the typical {001} (represent {001}, {010}, and {100}) and {111} surface of $\gamma$-$WO_3$ (Figure 7 and Table 3, detailed calculations and checks on the oxidation state of Cr and W can be found in Supporting Information section S1 and S2, respectively). Indicated by the surface energies and formation energies ($\Delta E_{form}$) listed in Table 3, the $(\sqrt{2} \times \sqrt{2})$R45 reconstruction of {001} was the most stable surface for $\gamma$-$WO_3$, which agreed well with reported simulations[44,45] and experiments that vapor phase methods usually obtain $\gamma$-$WO_3$ 1D nanostructures on substrates showing [001] growth direction along the length.[46−49] However, unlike heterogeneous growth of $WO_3$ 1D nanostructures on substrates, homogeneous free growth in DC[20]/RF[7] thermal plasma CVD showed unique crystal growth habit (thermodynamic property) and 0D octahedra (equilibrium forms) can be obtained. To exclude the influences of elements and groups from raw materials on the surfaces of $WO_3$, pure W powders were used as raw materials (10−15 $\mu$m, Beijing Xing Rong Yuan Technology Co., Ltd., China) and similar results were obtained (Figure S1, Supporting Information). The well understanding of unique thermodynamic properties of MOX in thermal plasma still needs further simulation and experimental studies on a series of MOX particles synthesized by RF thermal plasma (e.g., ZnO, $SnO_2$, NiO, $TiO_2$, etc.).

Similarly, under Cr-doped condition, the form energy ($\Delta E_{form}$) of {111} surfaces indicated easier formation of {111} than {001} surface, which is inconsistent with our experimental results.

Therefore, for $\gamma$-$WO_3$ and Cr-doped $\gamma$-$WO_3$ particles synthesized by RF thermal plasma, the growth mechanism cannot be simply explained by surface energies calculated via


DOI: 10.1021/am5081277
ACS Appl. Mater. Interfaces 2015, 7, 2856−2866

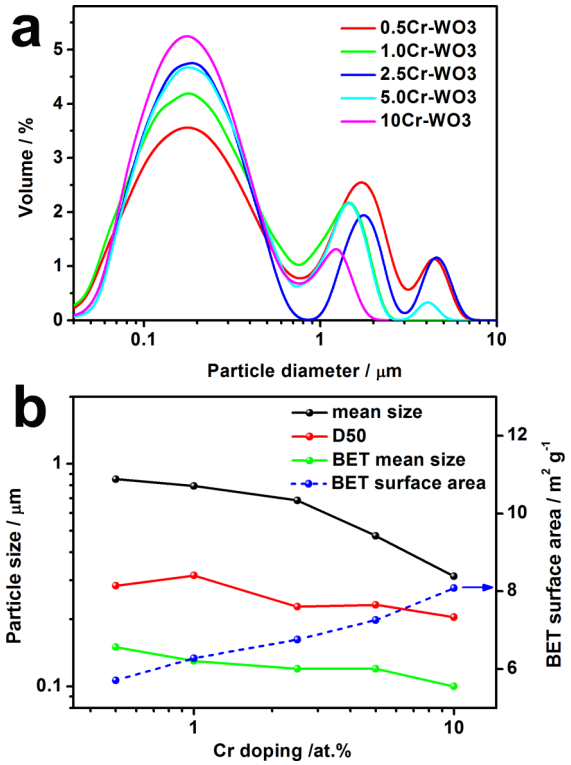


**Figure 5.** (a) Particle size distribution curves, (b) particle size comparison (black: mean size, red: D50, green: BET mean size), and BET surface areas comparison.

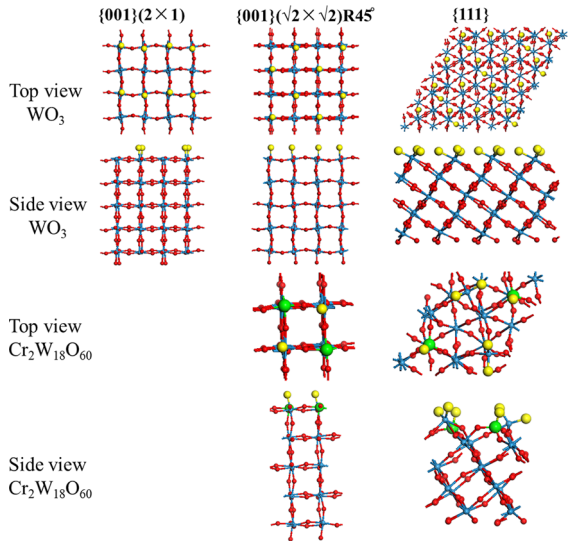


**Figure 7.** Relaxed surface structures for {001} and {111} surfaces of $\gamma$-$WO_3$ and Cr-doped $\gamma$-$WO_3$ (where the surface oxygens are colored yellow, bulk oxygens red, W ions blue, and Cr ions green).

**Table 3. Relaxed Surface Energies for the {001} and {111} Surfaces of $\gamma$-Monoclinic $WO_3$**

| surface | surface energy/ $J \cdot m^{-2}$ | $\Delta E_{form}$ (adsorption $O_2$)/eV | $\Delta E_{form}$ (doped Cr)/eV |
|---|---|---|---|
| {001}(2 × 1) | 1.55 | – | – |
| {001}($\sqrt{2} \times \sqrt{2}$)R45 | 1.49 | −0.23 | −1.39 |
| {111} | 1.72 | −0.20 | −2.18 |

simulations. Despite this, we can set crystal growth habits of pure $WO_3$ as an initial condition and then reconsider the role of Cr dopants on the morphology evolution.

In the beginning, $WO_3$ octahedra with {111} exposed facets formed due to fast growth rate along [001], [010], and [100] directions. The presence of Cr will cause distortion into the $WO_3$ matrix, repelling tungsten atoms from centric positions in $WO_6$ octahedra.[19,34,50] In addition, since the majority of the Cr

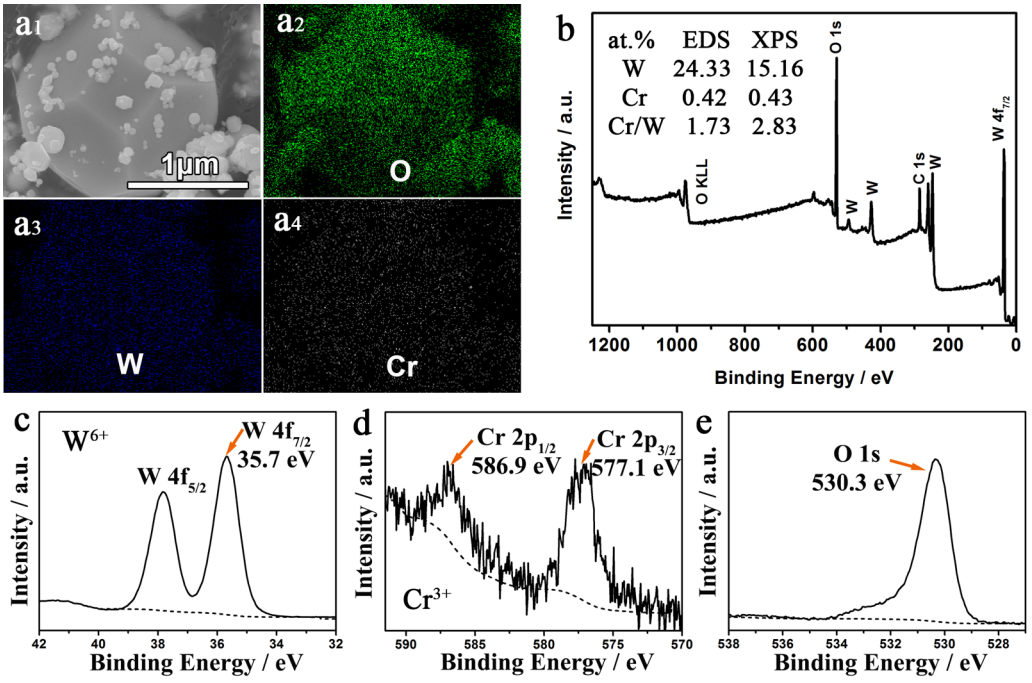


**Figure 6.** (a) EDS mapping images (O green, W blue, Cr white), (b) XPS spectrum, and (c–e) high-resolution XPS spectra of 2.5 at. % Cr-$WO_3$ at binding energies corresponding to W 4f, Cr 2p, and O 1s, respectively.



DOI: 10.1021/am5081277
ACS Appl. Mater. Interfaces 2015, 7, 2856–2866

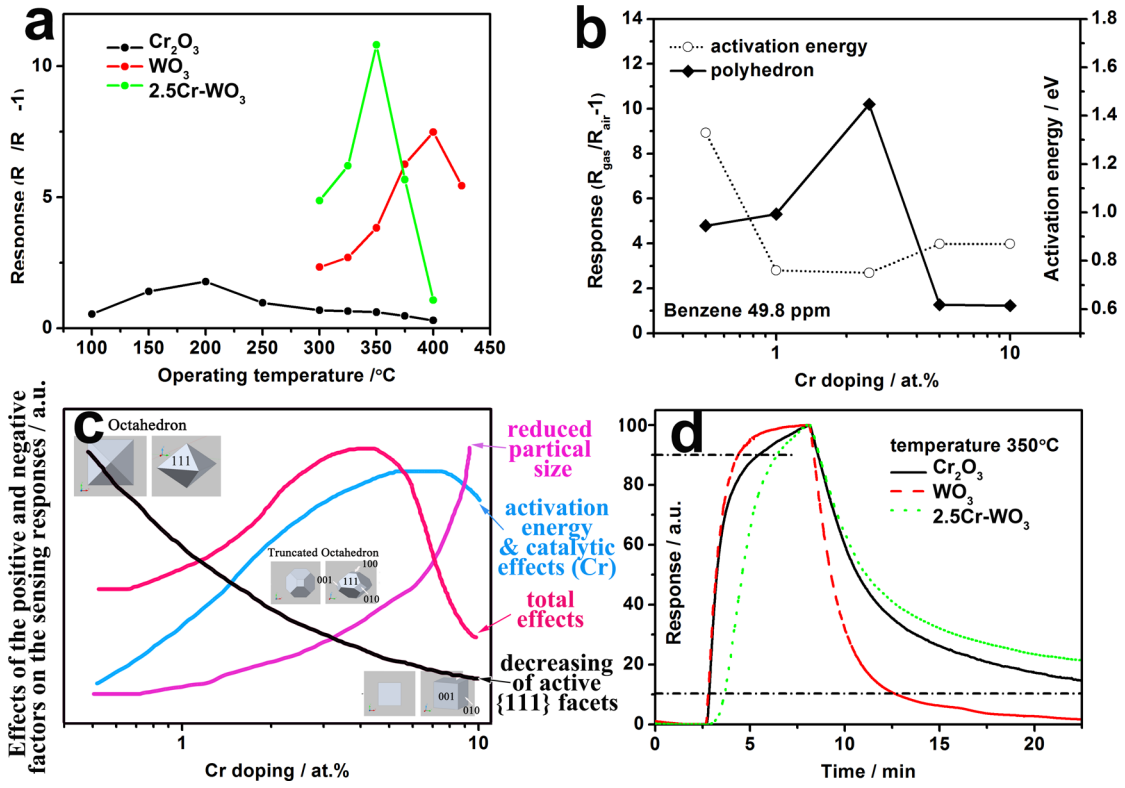


**Figure 8.** Gas sensing properties of Cr-doped $WO_3$ polyhedra (49.8 ppm benzene): (a) temperature-dependent responses comparison of $Cr_2O_3$ nanoparticles, $WO_3$ octahedra, and 2.5 at. % Cr-$WO_3$ polyhedra; (b) responses (solid line) and activation energies (dash line) comparison of $WO_3$ products (collector) doped with different atomic percentage of Cr; (c) the schematic illustration of effects of the positive and negative factors on the gas sensing responses; (d) response–recovery curves comparison of $Cr_2O_3$ nanoparticles, $WO_3$ octahedra, and 2.5 at. % Cr-$WO_3$ polyhedra.

atoms exist in the form of the Cr═O terminal bond according to Raman spectroscopy (Figure 3, also confirmed by EDS and XPS results in Figure 6), Cr atoms favor attachment on the particle surface to form chromates, which might form a chromate layer on the surface of $WO_3$ polyhedron[34] and thus might change the surface energies of different crystal facets similar to selective adsorption of capping or stabilizing agents used in liquid phase method.

Set crystal growth habits of pure $WO_3$ as an initial condition, the fundamental reason was attributed to coeffects of distortions introduced by Cr into the $WO_3$ matrix and a chromate layer on the crystal surface, which strongly affected the crystal growth by reducing the growth rates along [001], [010], and [100] directions. Cr dopant-controlled morphology evolution of $\gamma$-$WO_3$ from octahedron to cuboid has been evidenced by XRD patterns, SEM, TEM, and HRTEM images.

**3.2. Sensing Properties.** As we have mentioned in our previous work, gas sensing processes can be divided into three units, which are gas diffusion/molecule capture (utility factor and some case of receptor function), surface reaction (receptor function), and electron transport (transducer function).[29,51,52] Unit enhancements can significantly improve the sensing properties of the gas sensors.[7,29,31] For Cr-doped $WO_3$ polyhedra, exposed crystal facets, Cr doping, and particle size are key factors for sensing properties due to their effects on the surface reaction and electron transport units.

The crystallographic stacking of (111) planes of $\gamma$-$WO_3$ can be roughly taken as alternating stacking of W and O atoms,[19] which leaves dangling bonds of $W^-$ or $O^-$ on the surface (highly active crystal surface). It is the main reason why $WO_3$ octahedra bound by {111} facets showed good gas sensing properties.[7] Cr dopants brought two advantages on the sensing properties.

On one hand, the introduction of Cr dopants might contribute to the optimal temperature. We prepared $Cr_2O_3$ nanoparticles by decomposition of ammonium chromate in the same RF thermal plasma. Since the optimal operating temperature of $Cr_2O_3$ for benzene was 200 °C, the reduced optimal operating temperature of Cr-doped $WO_3$ from 400 to 350 °C can be attributed to coeffects of $Cr^{3+}$ and $W^{6+}$ when the benzene gas sensing reaction was conducted on the crystal surface (Figure 8a).

On the other hand, sensing responses were improved by proper doping of Cr. The doping of lower valence $Cr^{3+}$ at the site of $W^{6+}$ results in significant decrease of electron concentration or increase the sensor resistance (Supporting Information Figure S2, at least an order of magnitude). Since resistance (electron concentration) varies with operating temperature, its effect on sensing response is complicated.

Therefore, activation energy of semiconductor is employed to clarify the relationship between resistance (electron concentration) and response. At constant surface coverage or constant density of states, the activation energy of semiconductor can be calculated by the Arrhenius plot of the resistance[53−56]

$$\frac{1}{\sigma} = \frac{1}{\sigma_0}\exp\left(\frac{\Delta E}{kT}\right) \quad (1)$$

$$\ln\frac{1}{\sigma} = \ln\frac{1}{\sigma_0} + \frac{\Delta E}{kT} \quad (2)$$



DOI: 10.1021/am5081277
ACS Appl. Mater. Interfaces 2015, 7, 2856−2866

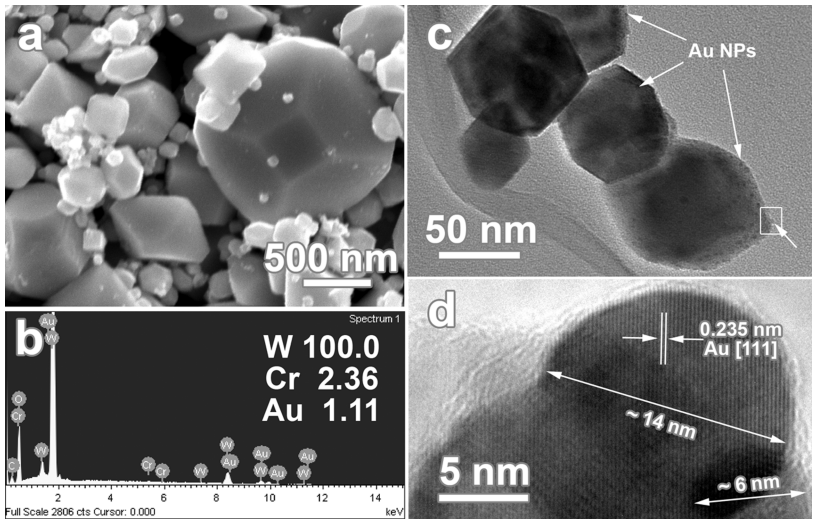


**Figure 9.** (a) SEM, (b) EDS, (c) TEM, and (d) HRTEM images of Au-decorated 2.5 at. % Cr-doped $WO_3$ truncated octahedra.

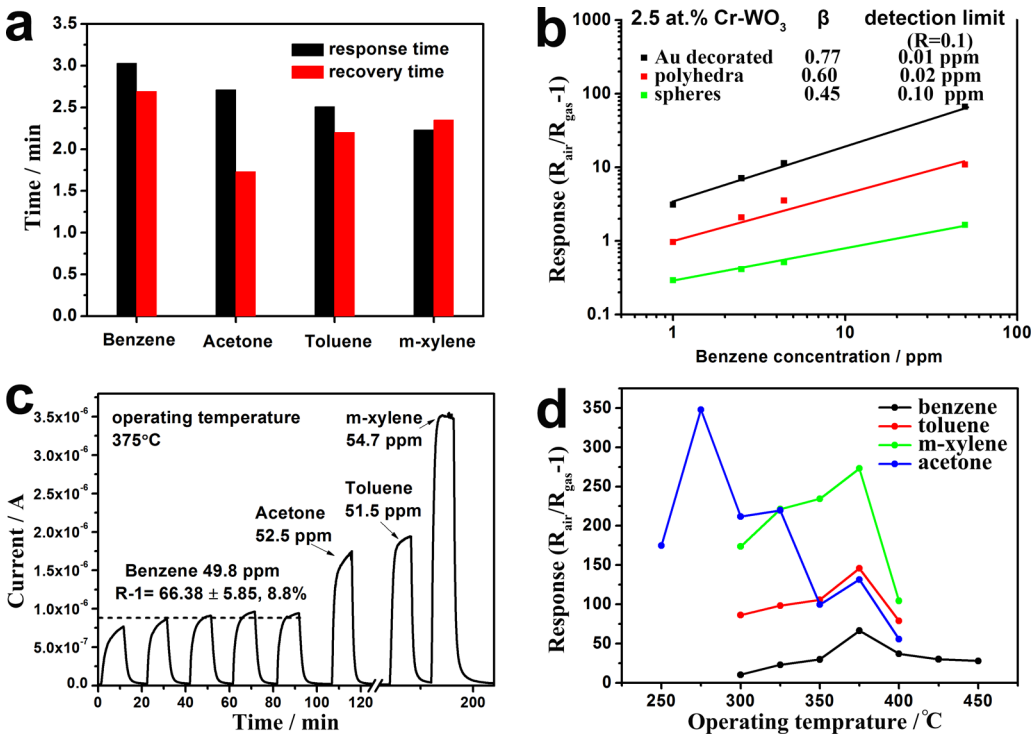


**Figure 10.** Gas sensing properties of Au-decorated 2.5 at. % Cr-$WO_3$ polyhedra: (a) response and recovery time; (b) log−log plots comparison of different 2.5 at. % Cr-$WO_3$ samples; (c) response−recovery curves, repeatability, and (d) responses to different kinds of VOCs at different operating temperature of Au-decorated 2.5 at. % Cr-$WO_3$ polyhedra.

where $\sigma$ denotes the conductance, $k$ is the Boltzmann's constant, $T$ is the absolute temperature, and $\Delta E$ is the activation energy. Plotting $\ln(1/\sigma)$ against $1/T$, $\Delta E$ can be obtained.

Sensing results in Figure 8b and c indicate that particle size, activation energy, and catalytic effects of Cr play major roles in improving the sensing responses when low percentage of Cr dopants was introduced, while crystal facets, activation energy, and catalytic effects of Cr reduce the sensing responses when high percentage of Cr dopants was introduced.

For the sample with low percentage of Cr dopants, the response to 49.8 ppm benzene gas increases with increasing Cr dopants due to stronger effect of reduced activation energy (caused by Cr dopants, dashed line of Figure 8b), particle size (Figure 5), and more edges of the crystal than decreasing percentage of highly active {111} facets (Figure 4). Moreover, it is reported that Cr can have a catalytic effect on the dissociation of BTX compounds into more active species of gases, and its enhancement for BTX sensing was confirmed.[57−59] Thus, chemical sensitization of Cr component on the surface contributed to the enhanced gas response to benzene in this work. In this case, activities of crystal facets had little effect on sensing responses.

When the effects of the positive and negative factors on the sensing responses were equal to each other, the highest response can be observed (2.5 at. % in this work), which was


DOI: 10.1021/am5081277
ACS Appl. Mater. Interfaces 2015, 7, 2856−2866

higher than that of pure $WO_3$ at its optimal operating temperature (400 °C).

Further increase of Cr dopants would result in sharp decrease of responses, which can be attributed to dominant effect of negative factors such as less active crystal facets (including less edges of the crystal, and nearly disappearing of highly active {111} facets, Figure 4 and 6), less active species formed by oxidation of the analytic gas before gas sensing reaction (caused by overdoping of Cr on the surface),[59] and higher activation energy (caused by overdoping of Cr, dashed line of Figure 8b). In this case, particle size had little effects on sensing responses.

Besides, one drawback of Cr-doped $WO_3$ that should be noted is the response time. Figure 8d shows that the response and recovery time of 2.5 at. % Cr-$WO_3$ polyhedra at 350 °C (3.72 and >15.0 min, respectively) are worse than those of $Cr_2O_3$ and $WO_3$ octahedra, which are also longer than our previous work on other metal oxide sensing materials (2.0−3.3 and <13 min at 350 °C for the same system, respectively).[7,29,31,53] It means that Cr will reduce the adsorption, reaction rate, and desorption of benzene gas on $WO_3$ surface (poor response and recovery time), although it can improve the efficiency (high sensing responses) and reduce the operating temperature.

To improve the adsorption, reaction rate, and desorption on the crystal surface, 2.5 at. % Cr-$WO_3$ polyhedra with the highest responses was chosen as the sample for Au decoration (Au loading, 1.11 at. %, Figure 9a and b).

High-magnification TEM images show that ultrasmall Au nanoparticles have been successfully decorated on the surfaces of 2.5 at. % Cr-$WO_3$ polyhedra (Figure 9c). The corresponding HRTEM image in Figure 9d shows two typical Au nanoparticles with a size of ∼6 and ∼14 nm, respectively. The spacing of 0.235 nm is consistent with the value for (111) plane of Au (space group: $Fm\bar{3}m$). The role of noble metals on MOX semiconductors was studied well in the past decade, and their enhancements on the surface reaction were mainly attributed to modify the sensing surface by enhancing the surface reaction due to their catalytic effects (high reaction rates and responses) and the additional depletion layers (high resistances).[60−63] As a result, the response and recovery time to VOCs were significantly improved to 2.2−3.0 and 1.7−2.7 min, respectively (Figure 10a, 350 °C), and the responses and detection limit were also promoted (Figure 10b, 350 °C).

According to the conductance model limited by the electron transport across the intergranular Schottky barrier,[64,65] the response equation of grain-based gas sensors,[60,64,66,67] we can obtained the following equation (for resistance decrease)[29]

$$\log(R_{air}/R_{gas} - 1) = \log A_g + \beta \log p_g \quad (3)$$

A $\beta$ value of 0.5 is generally indicative of a fully regular microstructure of the nanograins.[61] Disordered microstructure is expected to increase $\beta$ above this value, whereas local agglomeration or zones of the structure cause a reduction of $\beta$ below this value.[66,68] The $\beta$ values of both Cr-$WO_3$ polyhedra (0.60) and Au-decorated Cr-$WO_3$ polyhedra (0.77) were deduced significantly higher than 0.5 (Figure 10b), which might be due to the broad size distribution and nonspherical shape. The $\beta$ value of Cr-$WO_3$ spheres (0.45) was lower than 0.5, which might due to local agglomeration or zones of the film.

The enhanced surface reaction and electron transport units allow the sensitive and fast detection of VOCs with remarkable signal-to-noise ratio (Figure 10c). The responses to ppm-level benzene are remarkable and stable ($R_{49.8\ ppm}$ = 66.38 ± 8.8%). The sensor has a selective response to acetone at low temperature (275 °C), while it is more sensitive to BTX (benzene, toluene, *m*-xylene) at high temperature (375 °C, Figure 10d).

## 4. CONCLUSIONS

In summary, the synthesis of Cr-doped $WO_3$ polyhedra has been demonstrated. Kinetic factors showed little effects on the equilibrium morphology of Cr-doped $WO_3$ polyhedra, while equilibrium morphologies of $WO_3$ polyhedra can be controlled by thermodynamic factor (Cr doping). Set crystal growth habits of pure $WO_3$ as an initial condition, coeffects of distortions introduced by Cr into the $WO_3$ matrix, and a chromate layer on the crystal surface could reduce the growth rates along [001], [010], and [100] directions. As a result, the morphology evolution was turning out as the following order with increasing Cr dopants: octahedron−truncated octahedron−cuboid. 2.5 at. % Cr-doped $WO_3$ polyhedra exhibited the highest sensing response due to coeffects of exposed crystal facets, activation energy, catalytic effects of Cr and particle size on the surface reaction, and electron transport units. Au decoration can significantly improve the sensing responses, detection limit, and response−recovery properties of 2.5 at. % Cr-doped $WO_3$ polyhedra. This study provides an opportunity to synthesize polyhedra with specific exposed facets by tailoring crystal growth habits in RF thermal plasma. The interesting synthetic method may be used for a wide range of MOX synthesized by CVD.

## ■ ASSOCIATED CONTENT

### Supporting Information

Mean size calculated from the BET surface area, detailed calculations of surface energies and formation energies, checks on the oxidation state of Cr and W, $\gamma$-$WO_3$ octahedra synthesized by pure W powders, and resistances comparison of $WO_3$ products (collector) doped with different atomic percentage of Cr. This material is available free of charge via the Internet at http://pubs.acs.org.

## ■ AUTHOR INFORMATION

### Corresponding Authors

*E-mail: flyuan@ipe.ac.cn. Fax: +86-10-62561822. Tel.: +86-10-82544974.

*E-mail: fding@ipe.ac.cn. Fax: +86-10-62561822. Tel.: +86-10-82544925.

### Notes

The authors declare no competing financial interest.

## ■ ACKNOWLEDGMENTS

This project is financially supported by the National High Technology Research and Development Program of China (863) (No. 2010AA064903) and the National Science Foundation of China (NSFC 51402293). We thank Dr. B. Nath, at Fujian Institute of Research on the Structure of Matter, CAS, for his contributions on the language of the manuscript; and Dr. Mingyan Wu, Jiandong Pang, and Prof. Daqiang Yuan, at Fujian Institute of Research on the Structure of Matter, CAS, for their contributions on materials characterization.



DOI: 10.1021/am5081277
ACS Appl. Mater. Interfaces 2015, 7, 2856−2866

## REFERENCES


(1) Kuang, Q.; Wang, X.; Jiang, Z.; Xie, Z.; Zheng, L. High-Energy-Surface Engineered Metal Oxide Micro-and Nanocrystallites and Their Applications. *Acc. Chem. Res.* **2014**, *47*, 308−318.

(2) Chen, M.; Wu, B.; Yang, J.; Zheng, N. Small Adsorbate-Assisted Shape Control of Pd and Pt Nanocrystals. *Adv. Mater.* **2012**, *24*, 862−879.

(3) Han, X.; Han, X.; Li, L.; Wang, C. Controlling the Morphologies of $WO_3$ Particles and Tuning the Gas Sensing Properties. *New J. Chem.* **2012**, *36*, 2205−2208.

(4) Barnard, A. S. Direct Comparison of Kinetic and Thermodynamic Influences on Gold Nanomorphology. *Acc. Chem. Res.* **2012**, *45*, 1688−1697.

(5) Kang, L.; Fu, H.; Cao, X.; Shi, Q.; Yao, J. Controlled Morphogenesis of Organic Polyhedral Nanocrystals from Cubes, Cubooctahedrons, to Octahedrons by Manipulating the Growth Kinetics. *J. Am. Chem. Soc.* **2011**, *133*, 1895−1901.

(6) Hu, P.; Yuan, F.; Bai, L.; Li, J.; Chen, Y. Plasma Synthesis of Large Quantities of Zinc Oxide Nanorods. *J. Phys. Chem. C* **2007**, *111*, 194−200.

(7) Zhang, H.; Yao, M.; Bai, L.; Xiang, W.; Jin, H.; Li, J.; Yuan, F. Synthesis of Uniform Octahedral Tungsten Trioxide by RF Induction Thermal Plasma and Its Application in Gas Sensing. *CrystEngComm* **2013**, *15*, 1432−1438.

(8) Hu, P.; Bai, L.; Yu, L.; Li, J.; Yuan, F.; Chen, Y. Shape-Controlled Synthesis of ZnS Nanostructures: A Simple and Rapid Method for One-Dimensional Materials by Plasma. *Nanoscale Res. Lett.* **2009**, *4*, 1047−1053.

(9) Klepser, B. M.; Bartlett, B. M. Anchoring a Molecular Iron Catalyst to Solar-Responsive $WO_3$ Improves the Rate and Selectivity of Photoelectrochemical Water Oxidation. *J. Am. Chem. Soc.* **2014**, *136*, 1694−1697.

(10) Hou, Y.; Zuo, F.; Dagg, A. P.; Liu, J.; Feng, P. Branched $WO_3$ Nanosheet Array with Layered $C_3N_4$ Heterojunctions and $CoO_x$ Nanoparticles as a Flexible Photoanode for Efficient Photoelectrochemical Water Oxidation. *Adv. Mater.* **2014**, *26*, 5043−5049.

(11) Chen, X.; Zhou, Y.; Liu, Q.; Li, Z.; Liu, J.; Zou, Z. Ultrathin, Single-Crystal $WO_3$ Nanosheets by Two-Dimensional Oriented Attachment toward Enhanced Photocatalystic Reduction of CO2 into Hydrocarbon Fuels under Visible Light. *ACS Appl. Mater. Interfaces* **2012**, *4*, 3372−3377.

(12) Xu, D.; Jiang, T.; Wang, D.; Chen, L.; Zhang, L.; Fu, Z.; Wang, L.; Xie, T. pH-Dependent Assembly of Tungsten Oxide Three-Dimensional Architectures and Their Application in Photocatalysis. *ACS Appl. Mater. Interfaces* **2014**, *6*, 9321−9327.

(13) Kida, T.; Nishiyama, A.; Hua, Z.; Suematsu, K.; Yuasa, M.; Shimanoe, K. $WO_3$ Nanolamella Gas Sensor: Porosity Control Using $SnO_2$ Nanoparticles for Enhanced $NO_2$ Sensing. *Langmuir* **2014**, *30*, 2571−2579.

(14) Huang, K.; Pan, Q.; Yang, F.; Ni, S.; Wei, X.; He, D. Controllable Synthesis of Hexagonal $WO_3$ Nanostructures and Their Application in Lithium Batteries. *J. Phys. D: Appl. Phys.* **2008**, *41*, 155417.

(15) Shibuya, M.; Miyauchi, M. Efficient Electrochemical Reaction in Hexagonal $WO_3$ Forests with a Hierarchical Nanostructure. *Chem. Phys. Lett.* **2009**, *473*, 126−130.

(16) Liu, F.; Li, L.; Mo, F.; Chen, J.; Deng, S.; Xu, N. A Catalyzed-Growth Route to Directly Form Micropatterned $WO_2$ and $WO_3$ Nanowire Arrays with Excellent Field Emission Behaviors at Low Temperature. *Cryst. Growth Des.* **2010**, *10*, 5193−5199.

(17) Zhang, J.; Tu, J.-p.; Xia, X.-h.; Wang, X.-l.; Gu, C.-d. Hydrothermally Synthesized $WO_3$ Nanowire Arrays with Highly Improved Electrochromic Performance. *J. Mater. Chem.* **2011**, *21*, 5492−5498.

(18) Zheng, F.; Lu, H.; Guo, M.; Zhang, M. Effect of Substrate Pre-Treatment on Controllable Synthesis of Hexagonal $WO_3$ Nanorod Arrays and Their Electrochromic Properties. *CrystEngComm* **2013**, *15*, 5828−5837.

(19) Zhao, Z.-G.; Liu, Z.-F.; Miyauchi, M. Nature-Inspired Construction, Characterization, and Photocatalytic Properties of Single-Crystalline Tungsten Oxide Octahedra. *Chem. Commun.* **2010**, *46*, 3321−3323.

(20) Guo, Y.; Murata, N.; Ono, K.; Okazaki, T. Production of Ultrafine Particles of High-Temperature Tetragonal $WO_3$ by dc Arc Discharge in Ar−$O_2$ Gases. *J. Nanopart. Res.* **2005**, *7*, 101−106.

(21) Li, Y.; Bando, Y.; Golberg, D.; Kurashima, K. $WO_3$ Nanorods/Nanobelts Synthesized via Physical Vapor Deposition Process. *Chem. Phys. Lett.* **2003**, *367*, 214−218.

(22) Naik, A. J.; Warwick, M. E.; Moniz, S. J.; Blackman, C. S.; Parkin, I. P.; Binions, R. Nanostructured Tungsten Oxide Gas Sensors Prepared by Electric Field Assisted Aerosol Assisted Chemical Vapour Deposition. *J. Mater. Chem. A* **2013**, *1*, 1827−1833.

(23) Chen, D.; Hou, X.; Wen, H.; Wang, Y.; Wang, H.; Li, X.; Zhang, R.; Lu, H.; Xu, H.; Guan, S. The Enhanced Alcohol-Sensing Response of Ultrathin $WO_3$ Nanoplates. *Nanotechnology* **2010**, *21*, 035501.

(24) Ma, J.; Zhang, J.; Wang, S.; Wang, T.; Lian, J.; Duan, X.; Zheng, W. Topochemical Preparation of $WO_3$ Nanoplates through Precursor $H_2WO_4$ and Their Gas-Sensing Performances. *J. Phys. Chem. C* **2011**, *115*, 18157−18163.

(25) Li, X.-L.; Lou, T.-J.; Sun, X.-M.; Li, Y.-D. Highly Sensitive $WO_3$ Hollow-Sphere Gas Sensors. *Inorg. Chem.* **2004**, *43*, 5442−5449.

(26) Gu, Z.; Zhai, T.; Gao, B.; Sheng, X.; Wang, Y.; Fu, H.; Ma, Y.; Yao, J. Controllable Assembly of $WO_3$ Nanorods/Nanowires into Hierarchical Nanostructures. *J. Phys. Chem. B* **2006**, *110*, 23829−23836.

(27) Zhao, X.; Cheung, T. L. Y.; Zhang, X.; Ng, D. H. L.; Yu, J. Facile Preparation of Strontium Tungstate and Tungsten Trioxide Hollow Spheres. *J. Am. Ceram. Soc.* **2006**, *89*, 2960−2963.

(28) Chen, D.; Ye, J. H. Hierarchical $WO_3$ Hollow Shells: Dendrite, Sphere, Dumbbell, and Their Photocatalytic Properties. *Adv. Funct. Mater.* **2008**, *18*, 1922−1928.

(29) Yao, M.; Hu, P.; Cao, Y.; Xiang, W.; Zhang, X.; Yuan, F.; Chen, Y. Morphology-Controlled ZnO Spherical Nanobelt-Flower Arrays and Their Sensing Properties. *Sens. Actuators, B* **2013**, *117*, 562−569.

(30) Zhang, J.; Liu, X.; Wu, S.; Xu, M.; Guo, X.; Wang, S. Au Nanoparticle-Decorated Porous $SnO_2$ Hollow Spheres: A New Model for a Chemical Sensor. *J. Mater. Chem.* **2010**, *20*, 6453−6459.

(31) Yao, M.; Hu, P.; Han, N.; Ding, F.; Yin, C.; Yuan, F.; Yang, J.; Chen, Y. ZnO Micro-Windbreak for Enhanced Gas Diffusion. *Sens. Actuators, B* **2013**, *186*, 614−621.

(32) Calestani, D.; Mosca, R.; Zanichelli, M.; Villani, M.; Zappettini, A. Aldehyde Detection by ZnO Tetrapod-Based Gas Sensors. *J. Mater. Chem.* **2011**, *21*, 15532−15536.

(33) Yao, M.; Jin, H.; Li, J.; Ding, F.; Lu, C.; Hou, G.; Yuan, F. Catalyst-Free Synthesis of $\beta$-SiC Polyhedra and $\alpha$-SiC Nano-Platelets by RF Thermal Plasma. *Mater. Lett.* **2014**, *116*, 104−107.

(34) Wang, L.; Teleki, A.; Pratsinis, S.; Gouma, P. Ferroelectric $WO_3$ Nanoparticles for Acetone Selective Detection. *Chem. Mater.* **2008**, *20*, 4794−4796.

(35) Daniel, M.; Desbat, B.; Lassegues, J.; Gerand, B.; Figlarz, M. Infrared and Raman Study of $WO_3$ Tungsten Trioxides and $WO_3{\cdot}H_2O$ Tungsten Trioxide Tydrates. *J. Solid State Chem.* **1987**, *67*, 235−247.

(36) Arai, M.; Hayashi, S.; Yamamoto, K.; Kim, S. Raman Studies of Phase Transitions in Gas-Evaporated $WO_3$ Microcrystals. *Solid State Commun.* **1990**, *75*, 613−616.

(37) Weckhuysen, B. M.; Wachs, I. E.; Schoonheydt, R. A. Surface Chemistry and Spectroscopy of Chromium in Inorganic Oxides. *Chem. Rev.* **1996**, *96*, 3327−3350.

(38) Ashkarran, A.; Ahadian, M.; Ardakani, S. M. Synthesis and Photocatalytic Activity of $WO_3$ Nanoparticles Prepared by the Arc Discharge Method in Deionized Water. *Nanotechnology* **2008**, *19*, 195709.

(39) Shpak, A.; Korduban, A.; Medvedskij, M.; Kandyba, V. XPS Studies of Active Elements Surface of Gas Sensors Based on $WO_{3-x}$ Nanoparticles. *J. Electron Spectrosc. Relat. Phenom.* **2007**, *156*, 172−175.




DOI: 10.1021/am5081277
*ACS Appl. Mater. Interfaces* 2015, 7, 2856−2866

(40) Leftheriotis, G.; Papaefthimiou, S.; Yianoulis, P.; Siokou, A. Effect of the Tungsten Oxidation States in the Thermal Coloration and Bleaching of Amorphous $WO_3$ Films. *Thin Solid Films* **2001**, *384*, 298−306.
(41) Xiao, W.; Xie, K.; Guo, Q.; Wang, E. Growth and Electronic Structure of Cu on $Cr_2O_3$ (0001). *J. Phys.: Condens. Matter* **2003**, *15*, 1155.
(42) Werfel, F.; Brümmer, O. Corundum Structure Oxides Studied by XPS. *Phys. Scr.* **1983**, *28*, 92.
(43) Ikemoto, I.; Ishii, K.; Kinoshita, S.; Kuroda, H.; Alario Franco, M.; Thomas, J. X-ray Photoelectron Spectroscopic Studies of $CrO_2$ and Some Related Chromium Compounds. *J. Solid State Chem.* **1976**, *17*, 425−430.
(44) Oliver, P. M.; Parker, S. C.; Egdellb, R. G.; Jones, F. H. Computer Simulation of the Surface Structures of $WO_3$. *J. Chem. Soc., Faraday Trans.* **1996**, *12*, 2049−2056.
(45) Lambert-Mauriat, C.; Oison, V.; Saadi, L.; Aguir, K. Ab Initio Study of Oxygen Point Defects on Tungsten Trioxide Surface. *Surf. Sci.* **2012**, *606*, 40−45.
(46) Klinke, C.; Hannon, J. B.; Gignac, L.; Reuter, K.; Avouris, P. Tungsten Oxide Nanowire Growth by Chemically Induced Strain. *J. Phys. Chem. B* **2005**, *109*, 17787−17790.
(47) Naik, A. J.; Warwick, M. E.; Moniz, S. J.; Blackman, C. S.; Parkin, I. P.; Binions, R. Nanostructured Tungsten Oxide Gas Sensors Prepared by Electric Field Assisted Aerosol Assisted Chemical Vapour Deposition. *J. Mater. Chem. A* **2013**, *1*, 1827−1833.
(48) Li, L.; Zhang, Y.; Fang, X.; Zhai, T.; Liao, M.; Sun, X.; Koide, Y.; Bando, Y.; Golberg, D. $WO_3$ Nanowires on Carbon Papers: Electronic Transport, Improved Ultraviolet-Light Photodetectors and Excellent Field Emitters. *J. Mater. Chem.* **2011**, *21*, 6525−6530.
(49) Stoycheva, T.; Annanouch, F. E.; Gràcia, I.; Llobet, E.; Blackman, C.; Correig, X.; Vallejos, S. Micromachined Gas Sensors Based on Tungsten Oxide Nanoneedles Directly Integrated via Aerosol Assisted CVD. *Sens. Actuators, B* **2014**, *198*, 210−218.
(50) Zheng, H.; Ou, J. Z.; Strano, M. S.; Kaner, R. B.; Mitchell, A.; Kalantar-zadeh, K. Nanostructured Tungsten Oxide−Properties, Synthesis, and Applications. *Adv. Funct. Mater.* **2011**, *21*, 2175−2196.
(51) Yamazoe, N.; Shimanoe, K. New Perspectives of Gas Sensor Technology. *Sens. Actuators, B* **2009**, *138*, 100−107.
(52) Yao, M.; Ding, F.; Cao, Y.; Hu, P.; Fan, J.; Lu, C.; Yuan, F.; Shi, C.; Chen, Y. Sn Doped ZnO Layered Porous Nanocrystals with Hierarchical Structures and Modified Surfaces for Gas Sensors. *Sens. Actuators, B* **2014**, *201*, 255−265.
(53) Roy Morrison, S. Surface States due to Deposited Alkaline Earth Cations on ZnO. *Surf. Sci.* **1974**, *45*, 20−38.
(54) Stetter, J. R. A Surface Chemical View of Gas Detection. *J. Colloid Interface Sci.* **1978**, *65*, 432−443.
(55) Arakawa, T.; Kurachi, H.; Shiokawa, J. Physicochemical Properties of Rare Earth Perovskite Oxides Used as Gas Sensor Material. *J. Mater. Sci.* **1985**, *20*, 1207−1210.
(56) Madou, M. J.; Morrison, S. R. *Chemical Sensing with Solid State Devices*, 1st ed.; Academic Press: London, 1989.
(57) Muzart, J. Chromium-Catalyzed Oxidations in Organic Synthesis. *Chem. Rev.* **1992**, *92*, 113−140.
(58) Ma, H.; Xu, Y.; Rong, Z.; Cheng, X.; Gao, S.; Zhang, X.; Zhao, H.; Huo, L. Highly Toluene Sensing Performance Based on Monodispersed $Cr_2O_3$ Porous Microspheres. *Sens. Actuators, B* **2012**, *174*, 325−331.
(59) Jeong, H.-M.; Kim, H.-J.; Rai, P.; Yoon, J.-W.; Lee, J.-H. Cr-Doped $Co_3O_4$ Nanorods as Chemiresistor for Ultraselective Monitoring of Methyl Benzene. *Sens. Actuators, B* **2014**, *201*, 482−489.
(60) D'Arienzo, M.; Armelao, L.; Mari, C. M.; Polizzi, S.; Ruffo, R.; Scotti, R.; Morazzoni, F. Macroporous $WO_3$ Thin Films Active in $NH_3$ Sensing: Role of the Hosted Cr Isolated Centers and Pt Nanoclusters. *J. Am. Chem. Soc.* **2011**, *133*, 5296−5304.
(61) Xue, X.; Chen, Z.; Ma, C.; Xing, L.; Chen, Y.; Wang, Y.; Wang, T. One-Step Synthesis and Gas-Sensing Characteristics of Uniformly Loaded Pt@$SnO_2$ Nanorods. *J. Phys. Chem. C* **2010**, *114*, 3968−3972.
(62) Kolmakov, A.; Klenov, D. O.; Lilach, Y.; Stemmer, S.; Moskovits, M. Enhanced Gas Sensing by Individual $SnO_2$ Nanowires and Nanobelts Functionalized with Pd Catalyst Particles. *Nano Lett.* **2005**, *5*, 667−673.
(63) Dolbec, R.; El Khakani, M. A. Sub-ppm Sensitivity towards Carbon Monoxide by Means of Pulsed Laser Deposited $SnO_2$:Pt Based Sensors. *Appl. Phys. Lett.* **2007**, *90*, 173114−173116.
(64) Park, C. O.; Akbar, S. A. Ceramics for Chemical Sensing. *J. Mater. Sci.* **2003**, *38*, 4611−4637.
(65) Schierbaum, K. D.; Weimar, U.; Göpel, W.; Kowalkowski, R. Conductance, Work Function and Catalytic Activity of $SnO_2$-Based Gas Sensors. *Sens. Actuators, B* **1991**, *3*, 205−214.
(66) Scott, R. W. J.; Yang, S. M.; Chabanis, G.; Coombs, N.; Williams, D. E.; Ozin, G. A. Tin Dioxide Opals and Inverted Opals: Near-Ideal Microstructures for Gas Sensors. *Adv. Mater.* **2001**, *13*, 1468−1472.
(67) Scott, R. W. J.; Yang, S. M.; Coombs, N.; Ozin, G. A.; Williams, D. E. Engineered Sensitivity of Structured Tin Dioxide Chemical Sensors: Opaline Architectures with Controlled Necking. *Adv. Funct. Mater.* **2003**, *13*, 225−231.
(68) D'Arienzo, M.; Armelao, L.; Cacciamani, A.; Mari, C. M.; Polizzi, S.; Ruffo, R.; Scotti, R.; Testino, A.; Wahba, L.; Morazzoni, F. One-Step Preparation of $SnO_2$ and Pt-Doped $SnO_2$ as Inverse Opal Thin Films for Gas Sensing. *Chem. Mater.* **2010**, *22*, 4083−4089.


DOI: 10.1021/am5081277
*ACS Appl. Mater. Interfaces* 2015, 7, 2856−2866